

Article

Segmentation of Online Ferrograph Images with Strong Interference Based on Uniform Discrete Curvelet Transformation[†]

Leng Han ¹, Song Feng ^{1,*} , Guang Qiu ¹, Jiufei Luo ¹ , Hong Xiao ¹ and Junhong Mao ²

¹ School of Advanced Manufacture Chongqing University of Posts and Telecommunications, Chongqing 400065, China; hanleng@cqupt.edu.cn (L.H.); qiuguangxq@163.com (G.Q.); jiufeluo@gmail.com (J.L.); xiaohong@cqupt.edu.cn (H.X.)

² Key Laboratory of Education Ministry for Modern Design and Rotor-Bearing Systems, Xi'an Jiaotong University, Xi'an 710049, China; jhmao@xjtu.edu.cn

* Correspondence: fengsong@cqupt.edu.cn; Tel.: +86-023-62480054

[†] This paper is an extended version of Song Feng, Guang Qiu, Jiufei Luo and Junhong Mao's paper "Binarization Method for Online Ferrograph Image Based on Uniform Curvelet Transformation. In Proceedings of the 2018 International Conference on Sensing, Diagnostics, Prognostics, and Control (SDPC), Xi'an, China, 15–17 August 2018".

Received: 4 March 2019; Accepted: 26 March 2019; Published: 30 March 2019



Abstract: Through real-time acquisition of the visual characteristics of wear debris in lube oil, an on-line visual ferrograph (OLVF) achieves online monitoring of equipment wear in practice. However, since a large number of bubbles can exist in lube oil and appear as a dynamically changing interference shadow in OLVF ferrograms, traditional algorithms may easily misidentify the interference shadow as wear debris, resulting in a large error in the extracted wear debris characteristic. Based on this possibility, a jam-proof uniform discrete curvelet transformation (UDCT)-based method for the binarization of wear debris images was proposed. Through multiscale analysis of the OLVF ferrograms using UDCT and nonlinear transformation of UDCT coefficients, low-frequency suppression and high-frequency denoising of wear debris images were conducted. Then, the Otsu algorithm was used to achieve binarization of wear debris images under strong interference influence.

Keywords: ferrography; uniform discrete curvelet transformation; binarization

1. Introduction

The wear debris in lube oil are closely related to the wear state of the machines. The size and form of the debris can reflect the wear level and reveal the content and temperature rise of the particular material. Therefore, oil debris analysis has become an essential condition monitoring technique that is utilized to diagnose wear and serve as an early warning system. To realize online wear monitoring, many particle detection methods have developed rapidly [1]. The electromagnetic wear detection sensor and image wear detection sensor are commonly used in online debris monitoring. When metal particles pass through the detection coil, they change the inductance of the coil or the magnetic flux through the coil such that the electromagnetic debris sensor can detect the inductive voltage of the coil, which can be measured in real time to allow for abrasive particle monitoring [2–5]. For the image wear detection sensor, detection is mainly based on transmission imaging [6] and reflection imaging [7] with a high detection accuracy of up to 5 microns.

Online visual ferrography (OLVF) is an important image wear detection sensor. Separating ferromagnetic wear debris from lube oil using a high-gradient magnetic field, obtaining ferrograms using an image sensor, and extracting wear debris information, such as size, shape, and concentration,

by ferrogram, online visual ferrography (OLVF) achieves online equipment wear monitoring. Compared with online monitoring technology based on inductive sensors, ultrasonic transducers and electrostatic sensors [8], OLVF can directly obtain visual information of the wear debris, reflecting wear conditions and realizing the monitoring of wear debris with a large size range, which has been applied in the evaluation of the anti-wear properties of lube oils, in automotive engine bench tests, and in gear wear monitoring [9–11].

Wear debris image processing, as an important prerequisite for equipment wear monitoring, and has been widely studied in recent years. Wu et al. [12] studied the preprocessing method of wear debris images, conducted comparative analysis of the grayscale processing effects of wear debris images through different-colored spaces, discussed the application effects of the background subtraction method and automatic threshold value method in the segmentation of the wear debris image, and proposed a suitable quantitative description method for wear debris images. Roylance et al. [13] studied the binarization, denoising and edge tracking of wear debris images, and extracted the features of wear debris, such as size, shape, and edge details. Zhan et al. [14] studied preprocessing techniques for wear debris images, such as image smoothing, image filtering, and image binarization, and processed the actual images using the blank convolution method, which effectively reduced noise and simplified the data processing process. Hu et al. [15] improved image quality using two filtering methods, for the convenience of subsequent object segmentation and extraction. In addition, Stachowiak et al. [16] studied the application of wavelet analysis in the automatic debris classification system, which could achieve a more reliable diagnosis of mechanical health. Wang et al. [17], while using the combined watershed and improved ant colony algorithm to segment the particle images, demonstrated the possibility of accurate image segmentation, including large abnormal particles and a sedimentary chain. Afterwards, a nonreference evaluation method for the edge detection of wear particles in ferrographic images was proposed by Wang et al. [18]; the wear particles obtained by this method are similar to those observed by the human eye, meaning that the evaluation results are simultaneously objective and reasonable. Wu et al. [19] studied a method to detect dynamic particles, obtaining three-dimensional abrasive grain characteristics that provide a viable and reliable indication of wear debris characteristics for machine condition monitoring. Yuan et al. [20] classify the debris through the abrasive grain boundary signal obtained by a new radial concave deviation (RCD) method.

The above methods are mostly proposed for off-line ferrograms, which are not applicable for the processing of OLVF ferrograms. In a complete wear monitoring process, the acquired number of OLVF ferrograms is very large. To facilitate OLVF ferrogram storage, OLVF ferrogram resolution is low, leading to difficulty in the extraction of wear debris characteristics. Meanwhile, to adapt to the online monitoring environment of the industrial site, the OLVF's optical imaging system is simple and compact in structure such that the optical magnification (approximately 2 times) is considerably smaller than that of the ferroscopy microscope. Under this condition, the detailed information of the debris is limited, which leads to difficulty in extracting the particles' features. In addition, a large number of bubbles will be generated under the action of valves, oil pumps, and gears during the lube oil cycle. As shown in Figure 1, when OLVF is used to perform online sampling analysis of the gearbox, the bubble flows through the probe, appearing as a dynamically changing interference shadow. It is difficult to eliminate the interference shadow from the OLVF ferrogram using the traditional Otsu binarization method. The interference shadow is misidentified as wear debris, resulting in large errors in the extracted wear debris characteristics.

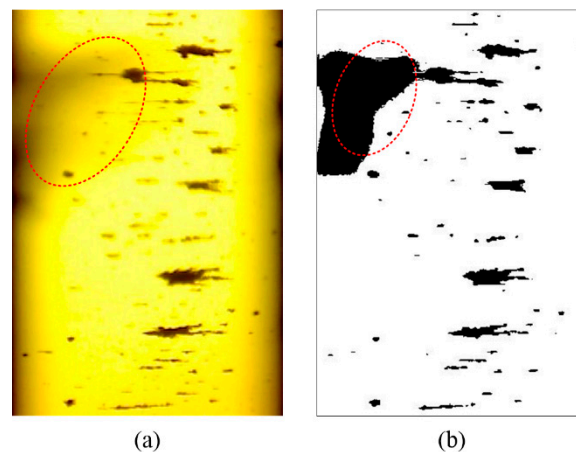


Figure 1. Effect of interference shadows on the binarization of on-line visual ferrograph (OLVF) ferrograms (shadow is encircled in red): (a) OLVF ferrogram; (b) results obtained by Otsu method.

In recent years, the curvelet transform has been of wide interest to domestic and foreign researchers because of its approximate optimal expression of line singularity features in images. The curvelet transform has been successfully applied to image denoising and fusion and has achieved good results [21]. The curvelet transform introduces directional parameters; therefore, it has better directivity than the two-dimensional wavelet transform. At the same time, the curvelet transform combines the advantages of the ridgelet transform in expressing linear features and the advantages of two-dimensional wavelets in expressing point features and is thus more suitable for multiscale analysis of images with high edge information. On this basis, the Fast Discrete Curvelet Transform (FDCT) was proposed by Candes et al. [22]. FDCT completely abandons the Ridgelet transform and directly gives the concrete expression of the Curvelet transform in the frequency domain. The image multiscale decomposition process by FDCT is as follows: the image is subjected to a fast Fourier transform; then, the frequency domain coefficients are resampled in different directions at different scales; finally, the fast Fourier transform is performed after the new coefficients are windowed, and the progeny coefficients of different scales in different directions can be obtained. Nguyen et al. [23] proposed Uniform Discrete Curvelet Transform (UDCT), the main idea of which was derived from FDCT and the filter bank-based Contourlet transform. Its implementation is mainly based on the FFT algorithm, but its curvelet function is designed in a multiscale filter bank structure. Compared with the Contourlet transform [24], UDCT has better frequency response, lower coefficient redundancy, and lower computational complexity, making it more suitable for engineering applications [25]. Feng et al. [26] used UDCT to analyze OLVF spectra at multi-scale. The nonlinear transformation is used to UDCT coefficients and achieve denoising of abrasive images, binary abrasive images under interference conditions were obtained, and has achieved good results.

2. Methods

2.1. Uniform Discrete Curvelet Transform

2.1.1. UDCTs Window Function

UDCT defines $2N + 1$ smooth curvelet window functions $u_l(\omega)$, $l = 0, 1, \dots, N$ to divide the frequency domain, where ω represents (ω_1, ω_2) . These window functions meet the following criteria:

- All window functions are considered to have a 2π period in both the ω_1 and ω_2 directions, and the domain of $u_l(\omega)$ is $[-\pi, \pi]^2$.
- As shown in Figure 2a, $u_0(\omega)$ is a square low-pass filter window with the support domain $[-\pi/2, \pi/2]^2$. Further, the support fields of the remaining $2N$ window functions are wedge-shaped.

- $u_l(\omega)$ is a smooth compact support function, and the central region function value is 1.
- $u_0(\omega) + \sum_{l=1}^{2N} [u_l(\omega) + u_l(\omega)] = 1$.

To construct $u_l(\omega)$, a one-dimensional projection function $\beta(t)$ was defined first, which smoothly transitioned from 0 to 1 in the range of $[-1, 1]$; parameters η_a and η_b were introduced to control the transition band width of $u_0(\omega)$ and $u_l(\omega)$, respectively. $u_0(\omega)$ is obtained by multiplying two one-dimensional functions, and $u_l(\omega)$ is constructed by multiplying a square window function and $2N$ angular functions.

$\beta(t)$ must meet the following requirements:

$$\begin{cases} \beta(t) = 1 & t \geq 1 \\ \beta(t) = 0 & t \leq -1 \\ \beta^2(t) + \beta^2(-t) = 1 & -1 < t < 1 \end{cases} \quad (1)$$

As shown in Figure 2b, $\beta(t)$ that satisfies the condition can be constructed as

$$\beta^2(t) = -\frac{5}{32}t^7 + \frac{21}{32}t^5 - \frac{35}{32}t^3 + \frac{35}{32}t + \frac{1}{2} \quad t \in [-1, 1] \quad (2)$$

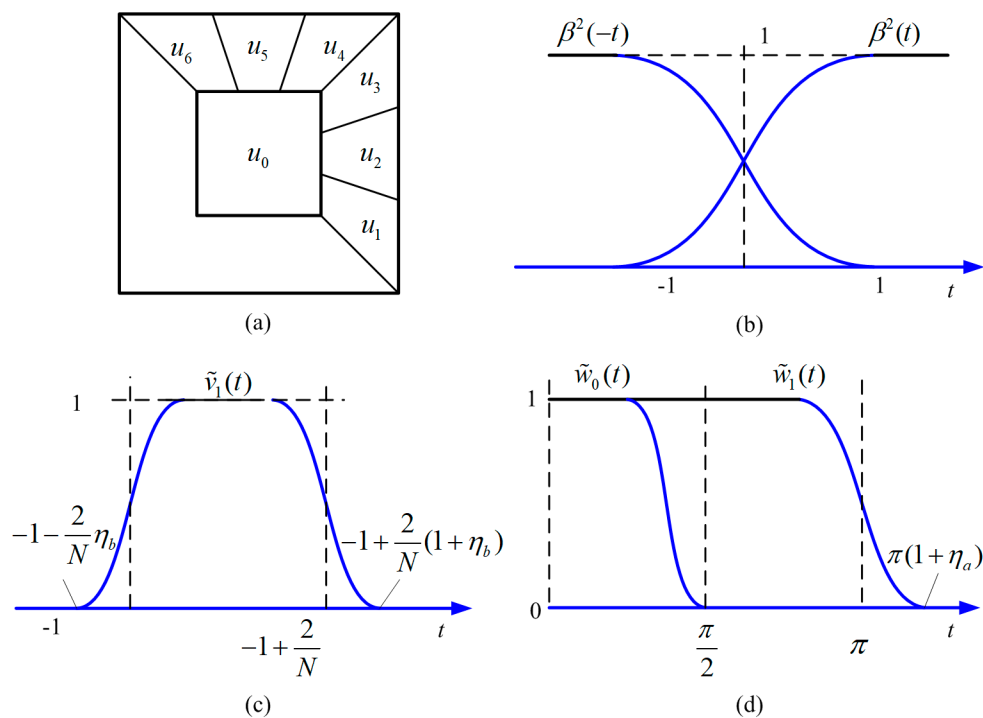


Figure 2. Structure of the Uniform Discrete Curvelet Transform (UDCT) window function: (a) Regions of essential support of $u_l(\omega)$ ($N = 3$); (b) One-dimensional smooth projection function; (c) Low-pass window function and the bandpass window function; (d) Angle window function.

Then, based on $\beta(t)$, $\tilde{w}_0(t)$ and $\tilde{w}_1(t)$ are defined as

$$\tilde{w}_1(t) = \beta\left(\frac{\pi - |t|}{\pi\eta_a}\right) \quad (3)$$

$$\tilde{w}_0(t) = \tilde{w}_1(2t(1 + \eta_a)) \quad (4)$$

where the support domain of $\tilde{w}_0(t)$ is $[-\pi/2, \pi/2]$. $\tilde{w}_0(t)$ and $\tilde{w}_1(t)$ are plotted in Figure 2d.

Thus, the expressions for the low-pass window function $w_0(\omega)$ and the bandpass window function $w_1(\omega)$ are defined as

$$w_0(\omega) = \tilde{w}_0(\omega_1)\tilde{w}_0(\omega_2) \quad (5)$$

$$w_1(\omega) = (1 - w_0^2(\omega))^{1/2} \tilde{w}_1(\omega_1)\tilde{w}_1(\omega_2) \quad (6)$$

Similarly, the angle window functions can be constructed as

$$v_1(t) = \beta\left(\frac{2/N - 1 - t}{2\eta_b/N}\right)\beta\left(\frac{t + 1}{2\eta_b/N}\right) \quad (7)$$

$$v_l(t) = v_1(t)(t - 2(l - 1)/N) \quad (8)$$

The square low-pass filter window $u_0(\omega)$ is constructed to a periodic $w_0(\omega)$. Additionally, the $2N$ wedge-shaped curved window function $u_l(\omega)$ can be obtained by periodic $v_l(\omega)$ and $w_1(\omega)$.

2.1.2. UDCT Frequency Domain Filter Bank

Suppose $N = k \cdot 2^n$, $k > 0$, $n \geq 0$. A UDCT frequency domain filter bank was constructed by $u_l(\omega)$. $2N + 1$ filters are defined as

$$\begin{cases} F_0(\omega) = 2u_0(\omega) \\ F_l(\omega) = 2^{\frac{n+3}{2}} u_l(\omega) \quad , \quad l = 1, \dots, 2N \\ G_l(\omega) = F_l(\omega) \end{cases} \quad (9)$$

where $F_0(\omega)$ is a low-pass filter, $F_l(\omega)$ is a directional filter, and $G_l(\omega)$ is a reconstruction filter that has the same form as the directional filter. The corresponding sampling matrix of the filter bank is

$$\begin{cases} D_0 = \text{diag}\{2, 2\}, \quad l = 0 \\ D_1 = \text{diag}\{2, 2^{n+1}\}, \quad l = 1, \dots, N \\ D_2 = \text{diag}\{2^{n+1}, 2\}, \quad l = N + 1, \dots, 2N \end{cases} \quad (10)$$

The specific structure of the UDCT filter bank is shown in Figure 3. 2D signal $x(n)$ is first filtered by $F_l(\omega)$, and the subband coefficients are obtained by downsampling. At the synthesis side, the subband coefficients are first upsampled, then convolved with $G_l(\omega)$. Finally, the reconstructed output signal is obtained by $y(n) = \text{Real}(\sum_{l=0}^{2N} x_l(\omega))$. To avoid frequency aliasing during down sampling, the window function parameters η_a and η_b should meet

$$\begin{cases} 0 < \eta_a \leq (\sqrt{17} - 3)/4 \\ 0 < \eta_b \leq 0.5 \\ 2(1 + \eta_a)(1 + 2\eta_b) \leq k \end{cases} \quad (11)$$

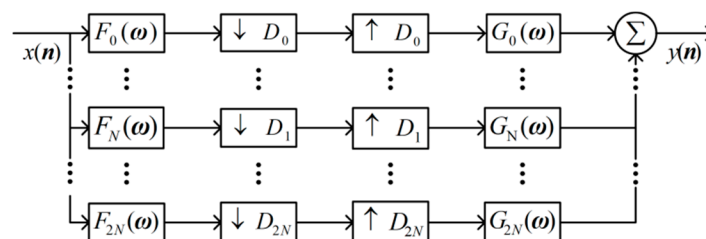


Figure 3. Structure of the UDCT filter bank.

2.2. Multiscale Decomposition of OLVF Ferrograms Based on UDCT

Multiscale and multidirectional decomposition of the OLVF ferrogram was performed using UDCT. Compared with image wavelet decomposition, UDCT not only has vertical, horizontal

and diagonal information but also has richer directional information. The OLVF ferrogram was decomposed by UDCT into a low-frequency part and a mid-high-frequency part. UDCT energy is mainly concentrated on the low-frequency coefficient that reflects the overview of the ferrogram. The mid-high-frequency coefficients mainly reflect the multidirectional edge feature information of the wear debris in the ferrogram. After gray processing of the ferrogram, shown in Figure 1, a six-layer UDCT was performed. Only the coefficient of the UDCT single-layer was retained, while the coefficients of the remaining layers were set to zero. The image was reconstructed to obtain a gray contour map of the reconstructed ferrogram, as shown in Figure 4. Obviously, the interference shadow is a low-frequency signal whose energy is mainly concentrated in low-frequency UDCT coefficients.

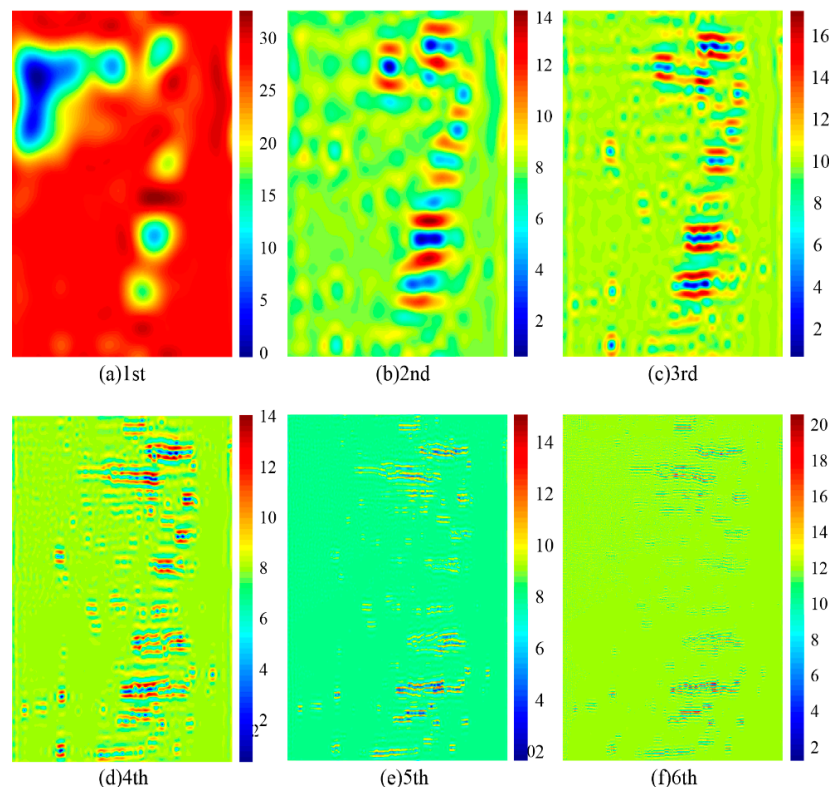


Figure 4. Contour single-layer coefficients from 1 to 6: (a) the first layer; (b) the second layer; (c) the third layer; (d) the fourth layer; (e) the fifth layer; (f) the sixth layer.

As shown in Figure 5, by removing the low-frequency coefficients, interference shadow in the ferrogram with small wear debris can be effectively removed. However, when there are large-sized debris in the ferrogram (Figure 6a), the gray value of the area covered by large debris changes only slightly, and the energy of the large debris after UDCT decomposition is mainly decomposed to low-frequency coefficients. This may be confused with low-frequency interference shadows. At this point, holes may be generated in the middle of large debris due to energy loss after removing the low-frequency coefficients, and erroneous binarization results are obtained (Figure 6b). When the size of the wear debris is small in the ferrogram, the wear debris image contains little low-frequency information. At this point, the interference shadow can be effectively removed by removing the low-frequency coefficient reconstructed ferrogram after UDCT decomposing without affecting the image characteristics of wear debris. However, when the size of the wear debris in the ferrogram is large, the wear debris image contains considerable low-frequency information. Consequently, the interference shadow cannot be eliminated by removing the low-frequency coefficient reconstructed ferrogram after UDCT decomposition due to a great loss of image characteristics of wear debris. Therefore low-frequency coefficient should be suppressed and transformed to a certain extent in order to achieve good interference shadow removal.

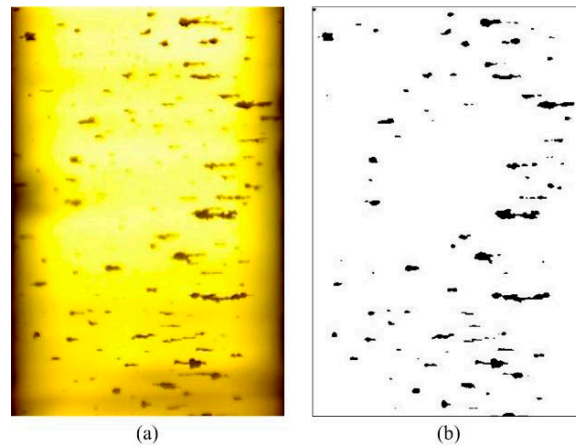


Figure 5. Results after removing low-frequency UDCT coefficients from a ferrogram with small wear debris. (a) on-line visual ferrograph (OLVF) ferrogram; (b) removing low-frequency coefficients after UDCT decomposition.

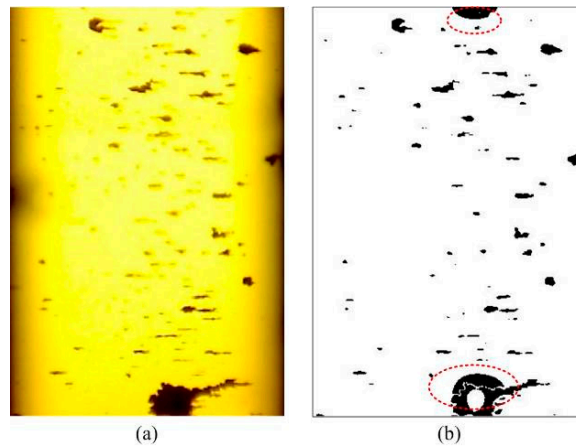


Figure 6. Results after removing low-frequency UDCT coefficients from a ferrogram with large wear debris (red circles show wrongly detected particles). (a) Large-size debris in the ferrogram; (b) erroneous binarization results.

2.3. Nonlinear Enhancement of OLVF Ferrogram Based on UDCT

A nonlinear function was used to process the low-frequency coefficients of the UDCT transform to eliminate the interference shadow information. The nonlinear function [27] is defined as follows:

$$f(x) = \frac{\text{sigm}[c(x - b)] - \text{sigm}[-c(x + b)]}{\text{sigm}[c(1 - b)] - \text{sigm}[-c(1 + b)]} \quad (12)$$

whereby $\text{sigm}(x) = 1/[1 + \exp(-x)]$; $0 < b < 1$, b is the input fragmentation threshold and c is the control coefficient of the enhanced data rate.

2.3.1. High-Frequency Denoising

High-frequency sub-band coefficients reflect the details and edge features of OLVF ferrograms and contain noise. The coefficients for UDCT were adjusted to achieve denoise processing of the OLVF ferrogram. The piecewise nonlinear adjustment function is

$$y = \begin{cases} s \cdot f(x), & x \geq T \\ 0, & x < T \end{cases} \quad (13)$$

where s is an adjustable coefficient; $x = |C(i, j)|/Max$; the noise evaluation parameter $\sigma = \text{median}(|C(i, j)|/0.6745)$; the threshold $T = \lambda \cdot \sigma$; the coefficient $\lambda = 3 \sim 4$; the adjusted high frequency progeny coefficient is $C_{Hnew}(i, j) = Max \cdot y$.

2.3.2. Low-Frequency Suppression

The interference shadows are found in the low frequencies, and the processing of low-frequency coefficients is the key. To suppress interference shadows, low-frequency progeny coefficients need to be suppressed. A piecewise nonlinear function was used to process the low-frequency progeny coefficients.

$$y = \begin{cases} s_1 \cdot f(x, c_1), & x \geq b \\ s_2 \cdot f(x, c_2), & x < b \end{cases} \quad (14)$$

where s_1 and s_2 are adjustable coefficients; $x = |C(i, j)|/Max$; $b = (\sum_{i=1}^M \sum_{j=1}^N |C(i, j)|) / (M \cdot N \cdot Max)$; $C(i, j)$ are the coefficients obtained by UDCT; Max is the largest absolute value for $C(i, j)$; and M and N are the matrix dimension. To ensure continuity of the piecewise function, $s_2 = s_1 \times f(b, c_1) / f(b, c_2)$. Then, the adjusted low frequency progeny coefficient is $C_{Lnew}(i, j) = Max \cdot y$.

The steps of the UDCT-based OLVF spectrum anti-interference binarization algorithm are as follows:

1. The background subtraction method is used to subtract the OLVF spectrum from the background spectrum, and grayscaled to obtain an OLVF spectrum that eliminates background interference;
2. The method of uniform discrete curvelet transform is performed on the OLVF spectrum to obtain a series of high-frequency and low-frequency progeny coefficients;
3. The nonlinear transformation of low-frequency progeny coefficients is segmented, and the low-frequency interference shadow energy is suppressed; then, the high-frequency progeny index is subjected to threshold denoising, with the remaining progeny coefficients unchanged;
4. The progeny coefficients are integrated to perform the inverse discrete curvelet inverse transform to obtain the OLVF spectrum after suppressing the interference shadow;
5. A binarization process is used on the processed spectral slice OLVF with automatic threshold iterative method.

The specific algorithm flow is shown in Figure 7.

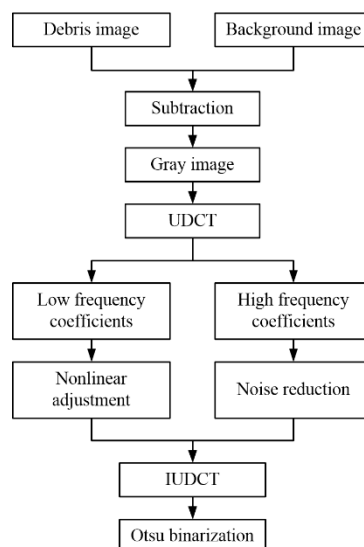


Figure 7. Spectral binarization based on uniform discrete curvelet transform.

3. Comparison with Other Methods

As shown in Figure 8, the proposed method was compared with three commonly used binarization methods: the Otsu method, the Kittler method, and the Niblack method. The calculation parameters of the proposed method are $c_1 = 5$, $s_1 = 0.45$, and $c_2 = 1$. As shown in Figure 1, the OLVF ferrogram has dark gray cloud-like interference shadows. The Otsu method can identify most of the wear debris in the ferrogram but also misidentifies the interference shadow at the bottom as wear debris. The Kittler method has good ability to identify low-contrast image objects. As a result, the part with dark gray shadows in the ferrogram is almost completely misidentified as wear debris. The Niblack method caused an intumescent effect on the ferrogram. The morphology of the wear debris binarized by the Niblack method is different from the actual one. The local interference shadows at the bottom of the ferrogram are misidentified as wear debris. Figure 8d shows the results obtained by the proposed method. The dark gray interference shadow is effectively removed, the edge of the wear debris image is clear, and the shape of the wear debris is similar to the actual shape.

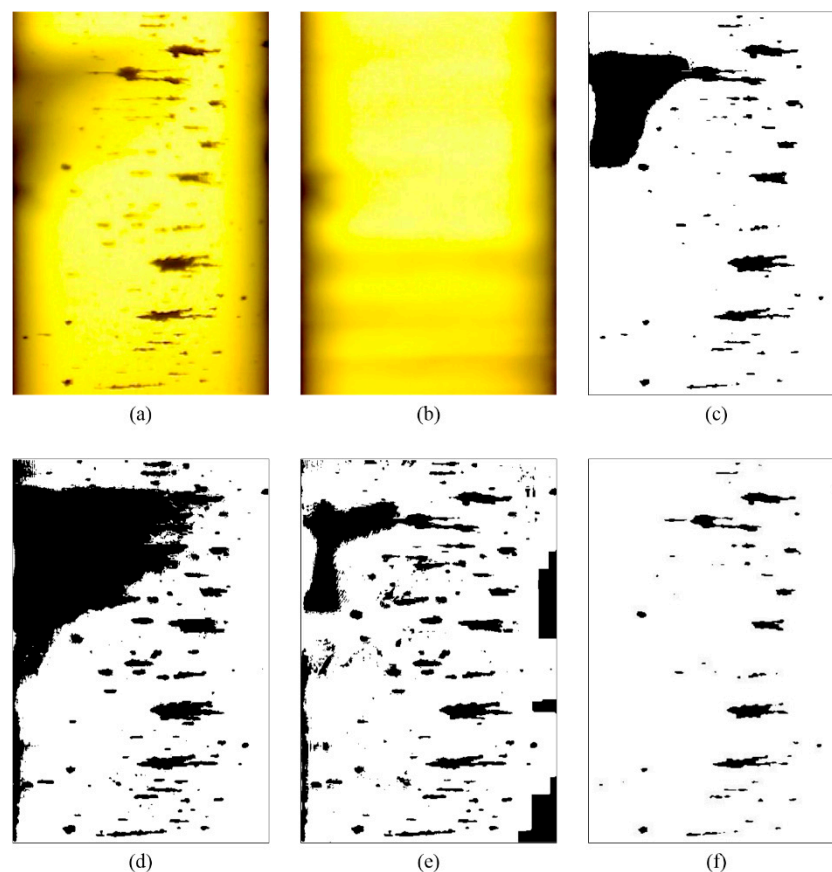


Figure 8. Comparison of the processing results of different binarization methods for a high-interference ferrogram. (a) Wear debris image of Figure 1a; (b) Background picture; (c) Otsu method; (d) Kittler method; (e) Niblack method; (f) the proposed method.

4. Application in Wear Monitoring of Gearbox

A gear wear experiment was conducted in a back-to-back setup, shown in Figure 9. The OLVF was used to monitor gear wear in real time. The test was carried out for 51.87 h. A total of 1557 OLVF ferrograms were obtained during the test.

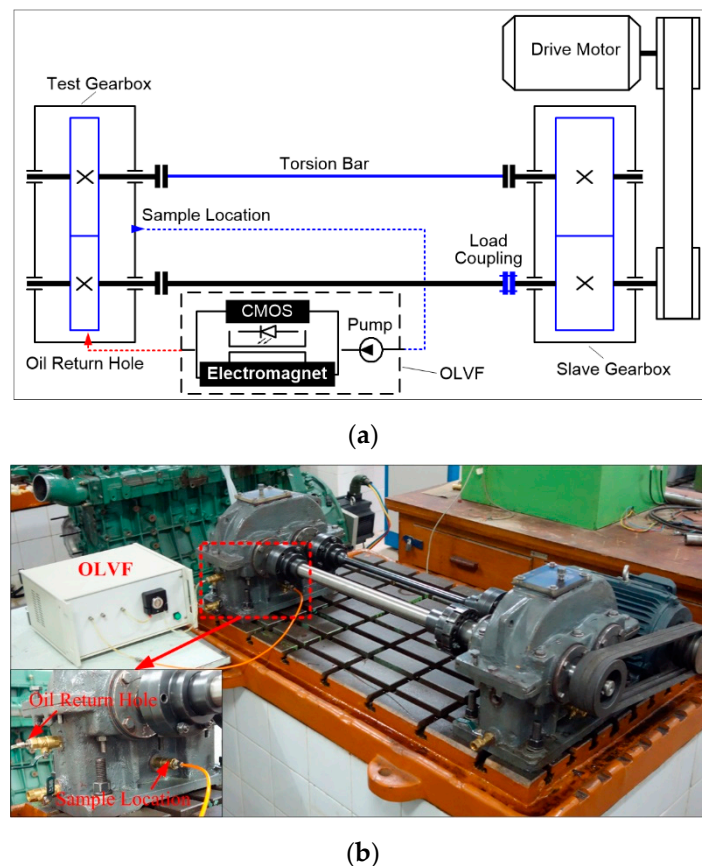


Figure 9. Back-to-back gear test rig: (a) schematic; (b) photograph.

Figure 10 shows representative OLVF ferrograms with bubble interference. Figure 11 shows typical OLVF ferrograms after 25 h. The OLVF ferrograms were segmented by the proposed method and the Otsu method, respectively. And the index of particle coverage area (IPCA) [26] was calculated by binarized OLVF ferrograms, and the variation of the IPCA curve was obtained, as shown in Figures 12 and 13. During the first five hours of the experiment, a large amount of bubbles was present in the lube oil due to the gear agitation. At this time, using the Otsu method to extract the IPCA values will produce large errors. There are many glitch impulses on the IPCA curve, as shown in Figure 13. Figure 14 is an image obtained by subtracting IPCA curves of the two methods. During the first five hours of the experiment, there have a great difference with the IPCA values extracted by this method and Otsu method. After about 30 h of experimentation, there is basically no difference in the experimental results of the two methods. Comparatively, the proposed method can better suppress the bubble interference existing in the OLVF ferrograms and reduce the IPCA glitch impulses generated by the bubbles, as shown in Figure 12. The bubbles in the lube oil are gradually reduced after 5 h, and both methods can obtain a good IPCA curve.

Obviously, IPCA has more glitch impulses before 5 h. The reason for this is because at the beginning of the experiment, bubbles are easily generated due to gear agitation because of the viscous lube oil. As the experiment progressed, the temperature of the lube oil increased and the viscosity decreased, and the generated bubbles were reduced, so that the interference of the bubbles on the OLVF spectrum was reduced.

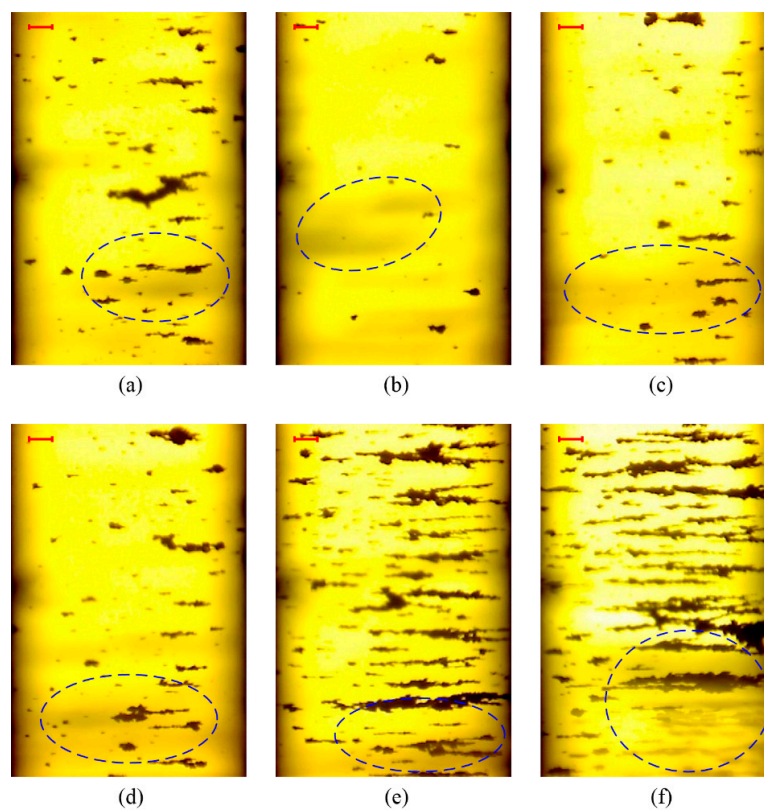


Figure 10. Representative ferrograms with interference shadows (the bar is 100 μm): (a) 22 min; (b) 2 h 26 min; (c) 4 h 6 min; (d) 5 h 8 min; (e) 16 h 6 min; (f) 21 h 50 min.

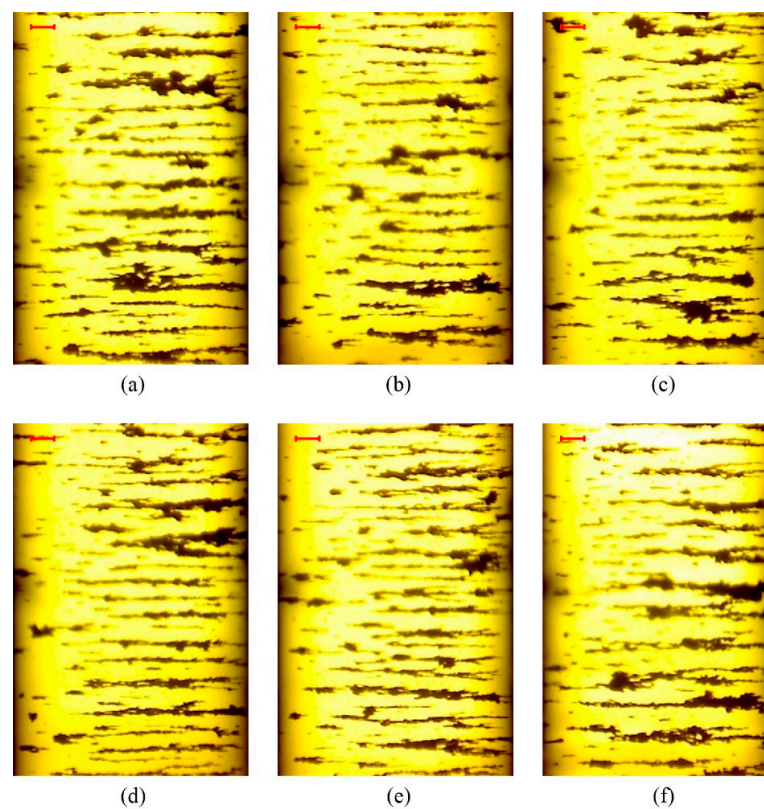


Figure 11. Representative ferrograms without interference shadows (the bar is 100 μm): (a) 25 h; (b) 30 h; (c) 35 h; (d) 40 h; (e) 45 h; (f) 50 h.

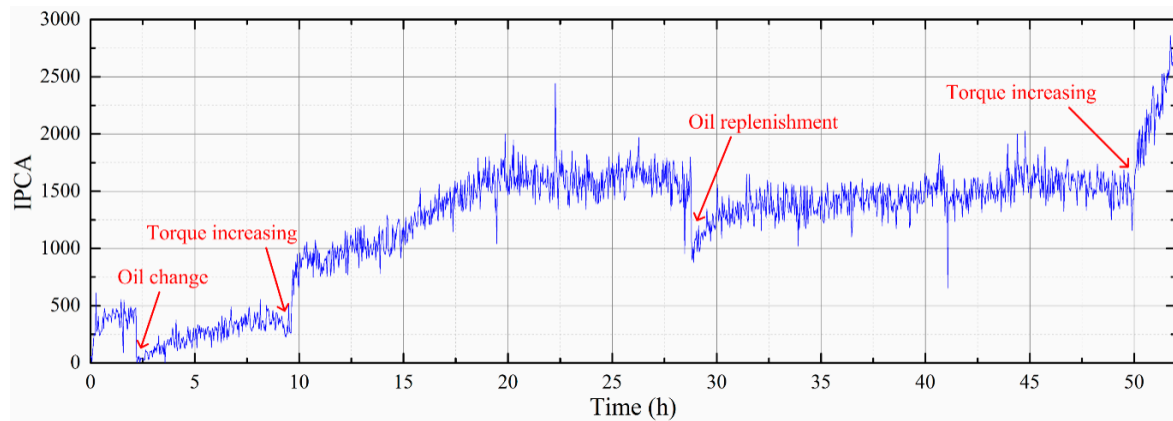


Figure 12. Variations of index of particle coverage area (IPCA) from the proposed method.

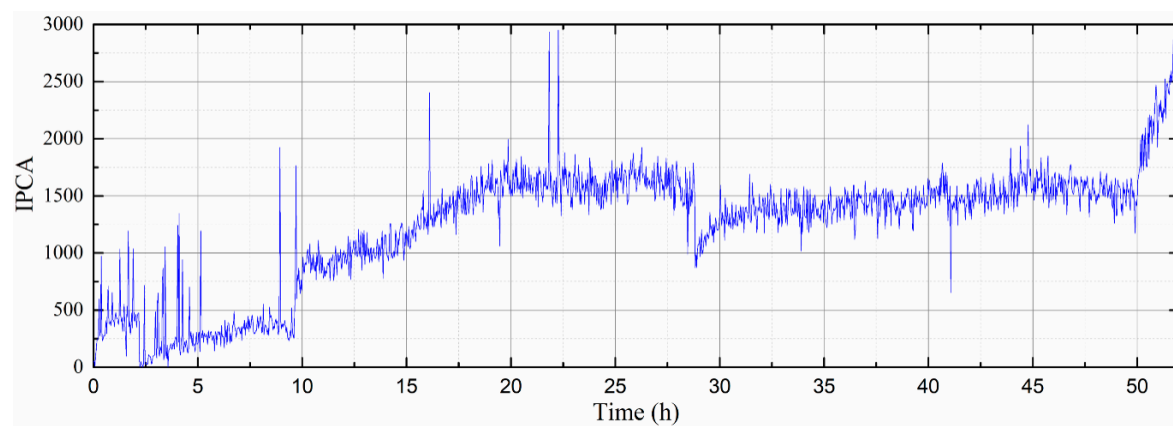


Figure 13. Variations of IPCA from the Otsu method.

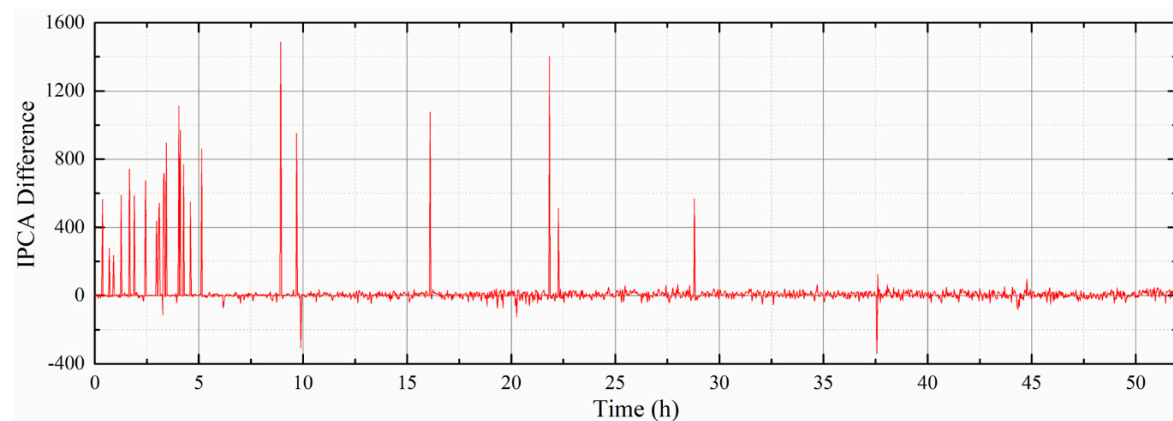


Figure 14. IPCA difference of two methods.

5. Conclusions

Multiscale analysis of OLVF ferrograms was performed using UDCT. Bubbles appear as a low frequency interference shadow in OLVF ferrograms. The proposed anti-interference segmentation method for the OLVF ferrograms was used to suppress the low-frequency coefficients of UDCT to eliminate interference shadow in the ferrograms. A wear debris image with a clear edge can be obtained. Additionally, the method is used in online gear wear monitoring. Additionally, the initial stage IPCA glitch impulses caused by bubbles can be effectively suppressed or eliminated. The proposed method can meet the requirements of OLVF online sampling analysis, which provides more accurate data for the subsequent extraction of wear debris characteristics.

Author Contributions: L.H., G.Q. and J.L. wrote the manuscript. H.X. analyzed the data. S.F. obtained the experimental data. After the manuscript was finished, J.M. reviewed the manuscript.

Funding: The financial support of the present research was provided by the National Science Foundation of China (Grant Nos. 51705057 and 51675408), the Science and Technology Research Project of Chongqing Municipal Education Commission (KJ1704108 and KJ1600430) and the Chongqing Science and Technology Commission (cstc2017jcyjAX0126 and cstc2015jcyjA70004). Finally, the authors are very grateful to the anonymous reviewers for their helpful comments and constructive suggestions.

Conflicts of Interest: The authors declare no conflicts of interest.

References

1. Zhu, X.; Zhong, C.; Zhe, J. Lubricating oil conditioning sensors for online machine health monitoring—A review. *Tribol. Int.* **2017**, *109*, 473–484. [[CrossRef](#)]
2. Centers, P.W.; Price, F.D. Real time simultaneous in-line wear and lubricant condition monitoring. *Wear* **1988**, *123*, 303–312. [[CrossRef](#)]
3. Flanagan, I.M.; Jordan, J.R.; Whittington, H.W. An inductive method for estimating the composition and size of metal particles. *Meas. Sci. Technol.* **1990**, *1*, 381. [[CrossRef](#)]
4. Hong, W.; Wang, S.; Tomovic, M.; Han, L.; Shi, J. Radial inductive debris detection sensor and performance analysis. *Meas. Sci. Technol.* **2013**, *24*, 5103. [[CrossRef](#)]
5. Hong, W.; Wang, S.; Tomovic, M.M.; Liu, H.; Wang, X. A new debris sensor based on dual excitation sources for online debris monitoring. *Meas. Sci. Technol.* **2015**, *26*, 095101. [[CrossRef](#)]
6. Mabe, J.; Zubia, J.; Gorritxategi, E. Photonic low-cost micro-sensor for in-line wear particle detection in flowing lube oils. *Sensors* **2017**, *17*, 586. [[CrossRef](#)]
7. Peng, Y.; Wu, T.; Wang, S.; Du, Y.; Kwok, N.; Peng, Z. A microfluidic device for three-dimensional wear debris imaging in online condition monitoring. *Proc. Inst. Mech. Eng. Part J J. Eng. Tribol.* **2017**, *231*, 965–974. [[CrossRef](#)]
8. Hong, W.; Cai, W.J.; Wang, S.P.; Tomovic, M.M. Mechanical wear debris feature, detection, and diagnosis: A review. *Chin. J. Aeronaut.* **2018**, *31*, 5–20. [[CrossRef](#)]
9. Feng, S.; Che, Y.; Mao, J.; Xie, Y.B. Assessment of antiwear properties of lube oils using online visual ferrograph method. *Tribol. Trans.* **2014**, *57*, 336–344. [[CrossRef](#)]
10. Cao, W.; Dong, G.; Xie, Y.; Peng, Z. Prediction of wear trend of engines via online wear debris monitoring. *Tribol. Int.* **2018**, *120*, 510–519. [[CrossRef](#)]
11. Feng, S.; Fan, B.; Mao, J.; Xie, Y. Prediction on wear of a spur gearbox by online wear debris concentration monitoring. *Wear* **2015**, *336–337*, 1–8. [[CrossRef](#)]
12. Wu, T.H.; Wang, J.Q.; Wu, J.Y.; Xie, Y.B.; Mao, J.H. Wear characterization by an online ferrograph image. *Proc. Inst. Mech. Eng. Part J J. Eng. Tribol.* **2011**, *225*, 23–34. [[CrossRef](#)]
13. Roylance, B.J.; Albidewi, I.A.; Laghari, M.S. Computer-aided vision engineering (CAVE)-quantification of wear particle morphology. *Lubr. Eng.* **1994**, *50*, 111–116.
14. Zhan, S.; Zheng, S.; Hu, X. Image preprocessing techniques for ferrographic spectrum analysis of wear abrasives. *J. He Fei Univ. Technol. Nat. Sci.* **2004**, *27*, 44–47.
15. Hu, X.; Huang, P.; Zheng, S. On the pretreatment process for the object extraction in color image of wear debris. *Int. J. Imaging Syst. Technol.* **2007**, *17*, 277–284. [[CrossRef](#)]
16. Stachowiak, G.W.; Podsiadlo, P. Towards the development of an automated wear particle classification system. *Tribol. Int.* **2006**, *39*, 1615–1623. [[CrossRef](#)]
17. Wang, J.; Zhang, L.; Lu, F.; Wang, X. The segmentation of wear particles in ferrograph images based on an improved ant colony algorithm. *Wear* **2014**, *311*, 123–129. [[CrossRef](#)]
18. Wang, J.; Bi, J.; Wang, L.; Wang, X. A non-reference evaluation method for edge detection of wear particles in ferrograph images. *Mech. Syst. Signal Process.* **2018**, *100*, 863–876. [[CrossRef](#)]
19. Yuan, W.; Chin, K.S.; Hua, M.; Dong, G.; Wang, C. Morphological feature extraction based on multiview images for wear debris analysis in online fluid monitoring. *Tribol. Trans.* **2016**, *60*, 408–418.
20. Yuan, W.; Chin, K.S.; Hua, M.; Dong, G.; Wang, C. Shape classification of wear particles by image boundary analysis using machine learning algorithms. *Mech. Syst. Signal Process.* **2016**, *72–73*, 346–358. [[CrossRef](#)]
21. Starck, J.L.; Candes, E.J.; Donoho, D.L. The curvelet transform for image denoising. *IEEE Trans. Image Process.* **2002**, *11*, 670–684. [[CrossRef](#)] [[PubMed](#)]

22. Candes, E.; Demanet, L.; Donoho, D.; Ying, L. Fast discrete curvelet transforms. *Multiscale Model. Simul.* **2006**, *5*, 861–899. [[CrossRef](#)]
23. Nguyen, T.; Chauris, H. Uniform discrete curvelet transform. *IEEE Trans. Signal Process.* **2010**, *58*, 3618–3634. [[CrossRef](#)]
24. Liu, M.; Yang, X. Image quality assessment using contourlet transform. *Opt. Eng.* **2009**, *48*, 107201. [[CrossRef](#)]
25. Bosman, R.; Schipper, D.J. Running-In of systems protected by additive-rich oils. *Tribol. Lett.* **2011**, *41*, 263–282. [[CrossRef](#)]
26. Feng, S.; Qiu, G.; Luo, J.F.; Mao, J.H. Binarization method for online ferrograph image based on uniform curvelet transformation. In Proceedings of the 2018 International Conference on Sensing, Diagnostics, Prognostics, and Control, Xi'an, China, 15–17 August 2018; pp. 314–319.
27. Wang, J.T. Theoretical and Experimental Study on Online Visualization-Ferrograph-Sensor. Ph.D. Thesis, Xi'an Jiaotong University, Xi'an, China, 2006.



© 2019 by the authors. Licensee MDPI, Basel, Switzerland. This article is an open access article distributed under the terms and conditions of the Creative Commons Attribution (CC BY) license (<http://creativecommons.org/licenses/by/4.0/>).